LA-UR-   08-5415

Title: Construction and characterization of ultraviolet acousto-optic modulator based femtosecond pulse shapers

Author(s): S. D. McGrane, M. Greenfield, and D. S. Moore

Intended for: Optics Express

Los Alamos
NATIONAL LABORATORY
———— EST.1943 ————

Form 836 (7/06)

Construction and characterization of ultraviolet acousto-optic modulator based femtosecond pulse shapers

S. D. McGrane,* M. Greenfield, and D. S. Moore

Los Alamos National Laboratory, Shock and Detonation Physics Group, MS P952, Los Alamos, NM 87545, USA
*Corresponding author: mcgrane@lanl.gov

Abstract: We present all the information necessary for construction and characterization of acousto optic pulse shapers, with a focus on ultraviolet wavelengths. Various radio-frequency drive configurations are presented to allow optimization via knowledgeable trade-off of design features. Detailed performance characteristics of a 267 nm acousto-optic modulator (AOM) based pulse shaper are presented. Practical considerations for AOM based pulse shaping of ultra-broad bandwidth (sub-10 fs) amplified femtosecond pulse shaping are described, with particular attention paid to the effects of the RF frequency bandwidth and optical frequency bandwidth on the spatial dispersion of the output laser pulses.

References and links

1. M. A. Dugan, J. X. Tull, and W. S. Warren, "High-resolution acousto-optic shaping of unamplified and amplified femtosecond laser pulses," JOURNAL OF THE OPTICAL SOCIETY OF AMERICA B-OPTICAL PHYSICS **14**, 2348-2358 (1997).
2. A. Monmayrant, and B. Chatel, "New phase and amplitude high resolution pulse shaper," Review of Scientific Instruments **75**, 2668-2671 (2004).
3. J. X. Tull, M. A. Dugan, and W. S. Warren, *High-Resolution ultrafast laser pulse shaping and its applications* (Academic Press, 1997).
4. M. M. Wefers, and K. A. Nelson, "ANALYSIS OF PROGRAMMABLE ULTRASHORT WAVE-FORM GENERATION USING LIQUID-CRYSTAL SPATIAL LIGHT MODULATORS," JOURNAL OF THE OPTICAL SOCIETY OF AMERICA B-OPTICAL PHYSICS **12**, 1343-1362 (1995).
5. A. M. Weiner, "Femtosecond pulse shaping using spatial light modulators," Review of Scientific Instruments **71**, 1929-1960 (2000).
6. M. M. Wefers, and K. A. Nelson, "GENERATION OF HIGH-FIDELITY PROGRAMMABLE ULTRAFAST OPTICAL WAVE-FORMS," OPTICS LETTERS **20**, 1047-1049 (1995).
7. A. M. Weiner, D. E. Leaird, J. S. Patel, and J. R. Wullert, "Programmable femtosecond pulse shaping by use of a multielement liquid-crystal phase modulator," Optics Letters **15**, 326-328 (1990).
8. F. Verluise, V. Laude, Z. Cheng, C. Spielmann, and P. Tournois, "Amplitude and phase control of ultrashort pulses by use of an acousto-optic programmable dispersive filter: Pulse compression and shaping," OPTICS LETTERS **25**, 575-577 (2000).
9. B. J. Pearson, and T. C. Weinacht, "Shaped ultrafast laser pulses in the deep ultraviolet," OPTICS EXPRESS **15**, 4385-4388 (2007).
10. M. Roth, M. Mehendale, A. Bartelt, and H. Rabitz, "Acousto-optical shaping of ultraviolet femtosecond pulses," Applied Physics B: Lasers and Optics **80**, 441-444 (2005).
11. H. Yu, and A. Dogariu, "Application of adaptive feedback loop for ultra-violet femtosecond pulse shaper control," OPTICS EXPRESS **14** (2006).
12. S. Coudreau, D. Kaplan, and P. Tournois, "Ultraviolet acousto-optic programmable dispersive filter laser pulse shaping in KDP," OPTICS LETTERS **31**, 1899-1901 (2006).
13. P. Nuernberger, G. Vogt, R. Selle, S. Fechner, T. Brixner, and G. Gerber, "Generation of shaped ultraviolet pulses at the third harmonic of titanium-sapphire femtosecond laser radiation," Applied Physics B: Lasers and Optics **88**, 519-526 (2007).
14. C. Schriever, S. Lochbrunner, M. Optiz, and E. Riedle, "19 fs shaped ultraviolet pulses," OPTICS LETTERS **31**, 543-545 (2006).

15. R. Selle, P. Nuernberger, F. Langhojer, F. Dimler, S. Fechner, G. Gerber, and T. Brixner, "Generation of polarization-shaped ultraviolet femtosecond pulses," OPTICS LETTERS **33**, 803-805 (2008).
16. S. Shimizu, Y. Nabekawa, M. Obara, and K. Midorikawa, "Spectral phase transfer for indirect phase control of sub-20-fs deep UV pulses," OPTICS EXPRESS **13**, 6345-6353 (2005).
17. D. Wolpert, M. Schade, F. Langhojer, G. Gerber, and T. Brixner, "Quantum control of the photoinduced Wolff rearrangement of diazonaphthoquinone in the condensed phase," JOURNAL OF PHYSICS B-ATOMIC MOLECULAR AND OPTICAL PHYSICS **41** (2008).
18. S.-H. Shim, D. B. Strasfeld, and M. T. Zanni, "Generation and characterization of phase and amplitude shaped femtosecond mid-IR pulses," OPTICS EXPRESS **14**, 13120-13130 (2006).
19. D. B. Strasfeld, S.-H. Shim, and M. T. Zanni, "Controlling vibrational excitation with shaped mid-IR pulses," PHYSICAL REVIEW LETTERS **99** (2007).
20. N. T. Form, R. Burbidge, J. Ramon, and B. J. Whitaker, "Parameterization of an acousto-optic programmable dispersive filter for closed-loop learning experiments," JOURNAL OF MODERN OPTICS **55**, 197-209 (2008).
21. A. Prakelt, M. Wollenhaupt, A. Assion, C. Horn, C. Sarpe-Tudoran, M. Winter, and T. Baumert, "Compact, robust, and flexible setup for femtosecond pulse shaping," Review of Scientific Instruments **74**, 4950-4953 (2003).
22. NeosTechnologies, "Introduction to acousto-optic modulators and deflectors."
23. R. Trebino, K. W. DeLong, D. N. Fittinghoff, J. N. Sweetser, M. A. Krumbugel, B. A. Richman, and D. J. Kane, "Measuring ultrashort laser pulses in the time-frequency domain using frequency-resolved optical gating," Review of Scientific Instruments **68**, 3277-3295 (1997).
24. T. Brixner, and G. Gerber, "Quantum control of gas-phase and liquid-phase femtochemistry," Chemphyschem **4**, 418-438 (2003).
25. E. C. Carroll, A. C. Florean, P. H. Bucksbaum, K. G. Spears, and R. J. Sension, "Phase control of the competition between electronic transitions in a solvated laser dye," Chemical Physics **350**, 75-86 (2008).
26. R. S. Judson, and H. Rabitz, "Teaching lasers to control molecules," Physical Review Letters **68**, 1500-1503 (1992).
27. R. J. Levis, and H. A. Rabitz, "Closing the loop on bond selective chemistry using tailored strong field laser pulses," Journal of Physical Chemistry A **106**, 6427-6444 (2002).
28. V. V. Lozovoy, and M. Dantus, "Coherent control in femtochemistry," Chemphyschem **6**, 1970-2000 (2005).
29. T. C. Weinacht, and P. H. Bucksbaum, "Using feedback for coherent control of quantum systems," Journal of Optics B: Quantum and Semiclassical Optics **4**, R35-52 (2002).
30. L. Gallmann, T. Pfeifer, P. M. Nagel, M. J. Abel, D. M. Neumark, and S. R. Leone, "Comparison of the filamentation and the hollow-core fiber characteristics for pulse compression into the few-cycle regime," APPLIED PHYSICS B-LASERS AND OPTICS **86**, 561-566 (2007).
31. C. P. Hauri, A. Guandalini, P. Eckle, W. Kornelis, J. Biegert, and U. Keller, "Generation of intense few-cycle laser pulses through filamentation - parameter dependence," OPTICS EXPRESS **13**, 7541-7547 (2005).
32. M. Nisoli, S. Stagira, S. De Silvestri, O. Svelto, S. Sartania, Z. Cheng, M. Lenzner, C. Spielmann, and F. Krausz, "A novel-high energy pulse compression system: generation of multigigawatt sub-5-fs pulses," Applied Physics B (Lasers and Optics) **B65**, 189-196 (1997).
33. T. Kobayashi, and A. Baltuska, "Sub-5 fs pulse generation from a noncollinear optical parametric amplifier," MEASUREMENT SCIENCE & TECHNOLOGY **13**, 1671-1682 (2002).
34. P. Baum, S. Lochbrunner, and E. Riedle, "Tunable sub-10-fs ultraviolet pulses generated by achromatic frequency doubling," OPTICS LETTERS **29**, 1686-1688 (2004).

1. Introduction

Femtosecond pulse shaping is the application of arbitrary phase and amplitude to individual spectral components of an ultrafast spectral light distribution. This is usually done by placing a programmable mask in the focal plane of a double subtractive spectrometer[1-5], as shown in Fig. 1. Typical programmable masks are liquid crystal spatial light modulators (SLM)[4-7] or acousto optic modulators (AOM)[1, 3]. Acousto optic programmable dispersive filters (AOPDFs)[8] are another method of femtosecond pulse shaping, which offer the benefits of inline use (no double subtractive spectrometer) but have other limitations, primarily damage threshold. Commercially available SLMs are not transparent to light at wavelengths less than 450 nm, so ultraviolet pulse shaping must be performed directly with an AOM[9-11], AOPDF[12] or indirectly by frequency doubling or sum frequency mixing with shaped 800 nm[13-17], which decreases conversion efficiency as the pulse shape becomes more complex. SLMs are opaque in the mid-infrared, where AOM pulse shaping has also been employed[18, 19]. AOM pulse shapers can be used at any wavelength that an acousto-optic crystal is available: quartz crystals for the UV[9, 10], tellurium dioxide for the visible to near

infrared[1, 3], and germanium in the mid-infrared[18, 19]. AOM pulse shaping was first performed by Warren and coworkers, and they have produced excellent reviews detailing the technique[1, 3].

An essential aspect of AOM pulse shaping that is not described in detail in the existing literature is how to choose and construct the radio-frequency (RF) generation components. While this is straightforward, it is a nontrivial procedure for most femtosecond laser users. Another noteworthy aspect of AOM pulse shaping that is not described in the literature is the relationship between the AOM RF frequency limitations and the limitations on spectral phase patterns that can be faithfully imposed on the diffracted optical wave; these limitations have been recently been considered for AOPDF pulse shaping[20]. We also compare the (dis)advantages of the multiple methods of RF generation currently available.

The three objectives of this paper are to 1) describe the construction and use of an AOM pulse shaper in sufficient detail to enable the average femtosecond laser user to easily build one, 2) measure the performance parameters for an ultraviolet pulse shaper at 267 nm, and 3) consider the limitations of AOM pulse shaping with sub-10 fs pulses of interest for future coherent control experiments
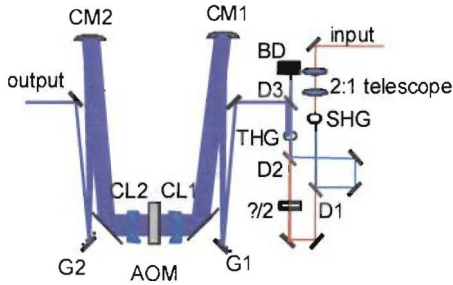
Fig. 1: Optical layout of 267 nm generation and pulse shaper. Input is 1 mJ, 110 fs, 800 nm. Output is 20 μJ, 120 fs (if unshaped) 267 nm. Energy at 267 nm into shaper is ~100 μJ. SHG = 0.25 mm Type I BBO θ=28⁰, φ=0⁰; THG = 0.25 mm Type I BBO θ=42⁰, φ=0⁰; D1 and D2 = dichroics that reflect 400 nm, transmit 800 nm; D3 = dichroic that reflects 267 nm, transmits 400 and 800 nm; BD = beam dump; CM1 and CM2 = concave spherical mirrors of 500 mm focal length; λ/2 = half waveplate at 800 nm; CL1 and CL2 = -25 mm cylindrical lenses for high energy pulse shaping; AOM = quartz acousto optic modulator crystal; G1 and G2 are 3600 g/mm gratings blazed at 240 nm.

2. Experimental Details and Results

2.1 Optical Layout:

The optical layout for the pulse shaper is shown in Fig. 1. The essential features are 1) spectral dispersion using a grating, 2) horizontal collimation and vertical focusing with the spherical mirror to produce a maximally spectrally resolved horizontal stripe at the focal plane; a short focal length negative cylindrical lens prevents tight focusing in the vertical direction to allow shaping of milliJoule (mJ) energy pulses, 3) the AOM, and 4) a mirror image of the input spectrometer. While pulse shaper designs exist that use true Littrow[21] (diffracted beam passes over input beam) orientation of the diffraction gratings, use of moderately long focal length spherical mirrors at the smallest possible angles allows simpler in-plane alignment without significant aberrations or loss of grating efficiency. The turning mirrors allow the AOM to be easily placed at the focal plane as well as easy transition between passive alignment of the AOM and alignment of the first diffracted order of the AOM at the Bragg angle, ~1 degree. The grating to spherical mirror distances and the spherical mirror to modulator distances equal the focal length, *f*, of the mirrors to achieve the

zero dispersion and zero spatial chirp of the "4-f" configuration[5]. The dispersion of the modulator material can be compensated by slightly adjusting the separation between the second spherical mirror-grating pair.

Each half of the pulse shaper is a simple spectrometer, but there are a few important considerations for the optical components within the shaper. Our goal was to use the shaper at 267 and 400 nm with a simple change of gimbal-mounted gratings (drop in and rotate). Optical losses in the UV can be quite significant, as many aluminum coated mirrors have poor reflectivity at 267 nm and each grating is <70% efficient; clearly aluminum or dielectric mirrors with high reflectivity at the wavelengths of interest must be used. The dispersion of the gratings necessary for the pulse shaper depends on the bandwidth that completely contains the pulse to the desired intensity threshold, the mirror focal length, the AOM crystal size, and grating availability. Calculating the dispersion length, $\Delta x_{dispersed}$, required for the AOM crystal is performed with Eqn. 1, assuming Littrow configuration (input angle, α = output angle, β) at the center wavelength, λ_{center}, which is approximately true for small deviations from the Littrow configuration.

$$
\begin{aligned}
\alpha = \beta_i &= \arcsin(10^{-6} gn\lambda_i / 2); \\
\Delta x_{dispersed} &= f \tan(\beta_{max} - \beta_{center}) + f \tan(\beta_{center} - \beta_{min})
\end{aligned}
\tag{1}
$$

The number of grating grooves per mm is g and the diffraction order is n. The focal length of the lenses or mirrors in mm is f, and λ_{min}, λ_{center}, and λ_{max} are the wavelengths in nm. These wavelengths are dispersed across $\Delta x_{dispersed}$, which should be close to the length of the modulator. Exact calculations for the off Littrow configuration use the grating equation, $\sin(\alpha)+\sin(\beta)=10^{-6}gn\lambda$, to solve for β, if necessary.

For initial alignment, the modulator is inactive (no RF pulse). Alignment proceeds with the gratings rotated to first order. Then the AOM is activated and the AOM's first order diffraction spot can be aligned. Achieving AOM diffraction requires overlap of the acoustic and optical waves, accomplished by vertical translation of the AOM at the spectrometer focal plane. Once weak diffraction is observed, the first turning mirror is adjusted (rotated in the horizontal plane) to maximize the diffracted intensity by achieving the Bragg angle. The second turning mirror and second spherical mirror can then be adjusted to return the diffracted beam down the center axis. Finally, pulse compression can be fine tuned by translation of the second grating to optimize a nonlinear signal such as second harmonic generation.

Note that optical damage of the AOM can occur even for dispersed beams. Spherical lenses alone will focus the beam in the vertical dimension to a spot size of a few tens of microns. We have experienced damage due to introduction of >100 μJ at 267 or 400 nm in a fused silica AOM and >400 μJ at 800 nm in a TeO$_2$ AOM for the pulse shaper design of Fig. 1, where f_1=500 mm, without the negative cylindrical lenses. The addition of f_2 = -25 mm focal length negative cylindrical lenses to collimate the beam through the AOM allows much higher beam energies. The beam waist is enlarged from $\lambda\sqrt{2}f_1/(d\pi)$ (with no cylindrical lens) to $-df_2/f_1$, where d is the input diameter. Collimating the beam size at the size of the acoustic wave, ~1 mm, allows a factor of 10-100 increase in energy through the AOM allowing mJ energy pulse shaping.

The particular specifications of the optical layout of Fig. 1 include: a) 0.5x telescope to optimize the frequency conversion efficiency of the BBO crystals; i.e. ~35% doubling efficiency in 5x5x0.25 mm second harmonic generation BBO and ~30% tripling efficiency in 5x5x0.25 mm third harmonic generation BBO (United Crystals); b) 400/800 nm dichroics (ThorLabs FM04 UV cold mirror); c) 267 reflected/400,800 nm transmitted dichroics (CVI), which is swapped with an Al mirror for 400 nm pulse shaping; d) high reflectivity 2" diameter

spherical mirrors coated for 267, 400, and 800 nm reflectivity (CVI DS-800/400/266-SMCC-2037-1.00-UV-0); e) 3" x 1 " aluminum turning mirrors (CVI PAUV coating); f) AOM (Neos Technologies fused silica 46200-6-1.5/50-.325, 43% efficient with spherical mirror focusing at 267 nm, Brimrose FSD8-200-100.400 fused silica, or Neos 15200-40 tellurium dioxide for 800 nm); and g) gratings with 67% absolute efficiency at 267 nm at s and p polarizations (Newport 53004BK01-170R). The data shown were recorded with input pulses centered at ~266-270 nm, >120 fs duration, 0.1 mJ energy, and ~3 mm FWHM beam size, using the Neos fused silica AOM unless otherwise noted.

2.2 AOM specifications:

AOM crystals appropriate for pulse shaping are available from several commercial suppliers. The AOM should be sufficiently long in the dispersion plane that there is potential for high resolution pulse shaping, but short enough that attenuation and dispersion of the RF wave is acceptable, ~50 mm for a few tens of percent loss in diffraction efficiency across the length of the crystal. The total number of effective pixels determines the complexity of optical pulses that can be generated, and is given by the time-bandwidth product of the AOM. The time bandwidth product is the ratio of the time it takes an acoustic pulse to travel across the entire crystal to the available acoustic feature size[1, 3].

The acoustic feature size is determined by the range of RF frequencies employed and the limitations of the RF generation at the AOM transducer. An RF wave centered at $\omega_{RF} = 200$ MHz with a bandwidth of $\Delta\omega_{RF} = 100$ MHz will have a minimum feature size of $\Delta t_{RF} = 1/\Delta\omega_{RF} = 10$ ns. The acoustic wave travels across the crystal of length l at the speed of sound $u_{acoustic}$ (4-6 mm/μs) in the time $t_{RF} = l/u_{acoustic}$, typically several μs. The maximum number of effective pixels is $t_{RF}/\Delta t_R$, assuming that the AOM is spectrally filled and that the optical spectral resolution is sufficient to resolve the minimum RF feature size. Each effective pixel is essentially the resolution element over which phase or amplitude changes can be transferred onto the optical pulse.
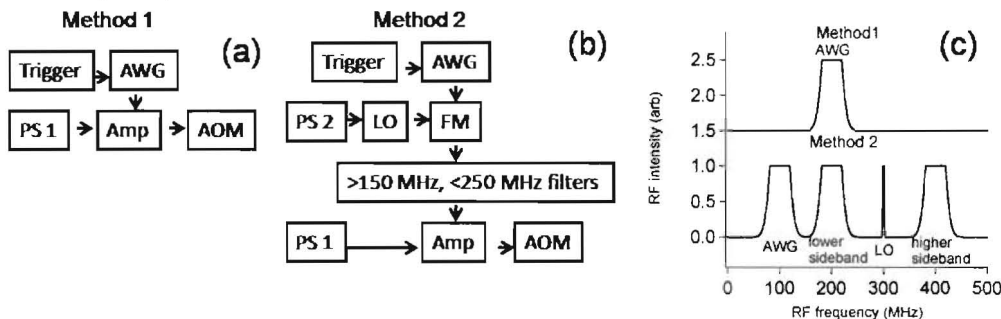

Fig. 2: RF diagram for electronics. The trigger synchronizes the acoustic generation to the optical pulse. AWG = computer controlled arbitrary waveform generator; PS1= 24 VDC 3A power supply; Amp = 6 W amplifier; AOM = acousto optic modulator; LO = 300 MHz voltage controlled local oscillator; FM = frequency mixer, PS2 = 12 VDC 20 mA power supply. Method 1 is direct RF shaping (a), Method 2 is sideband RF shaping (b), frequency diagrams of Methods 1 and 2 (c).

2.3 Shaped RF generation

The generation of shaped RF is, to ultrafast laser spectroscopists, the step that involves the largest unfamiliarity. There are 3 general strategies: 1) performing all of the shaping directly with a single arbitrary waveform generator (AWG)[18, 19], 2) shaping a low frequency wave with a single AWG and mixing it with a high frequency sine wave to form a higher frequency shaped waveform, or 3) shaping the real and imaginary parts of the RF separately with two

AWGs and performing In-phase/Quadrature (I/Q) mixing, as suggested in References [1, 3]; Since Method 2 has the same advantages as Method 3 with greater simplicity and less cost, only Methods 1 and 2 will be detailed in this paper.

Method 1 is diagrammed in Fig. 2a. The only RF electronics are the AWG and amplifier. This method is the simplest both conceptually and experimentally. However, the frequency range of the AOM must be commensurate with the frequency range of the AWG. A 500 MHz AWG will produce only 1 point every 2 ns, so a 250 MHz optical wave would have only 4 points per cycle- the wave may not be as smooth as desired in amplitude if the AWG frequency is not significantly larger than the highest RF frequency needed. This effect is illustrated in Fig. 3 for various frequencies. Cost could then constrain one to a lower center RF frequency, lower frequency bandwidth, and a smaller time-bandwidth product resulting in a less effective pulse shaper. We found that a 1 gigasample per second (GS/s) AWG can support 250 MHz pulse shaping, but a 500 MS/s AWG has aliasing problems at 250 MHz, as seen in Fig. 3a.
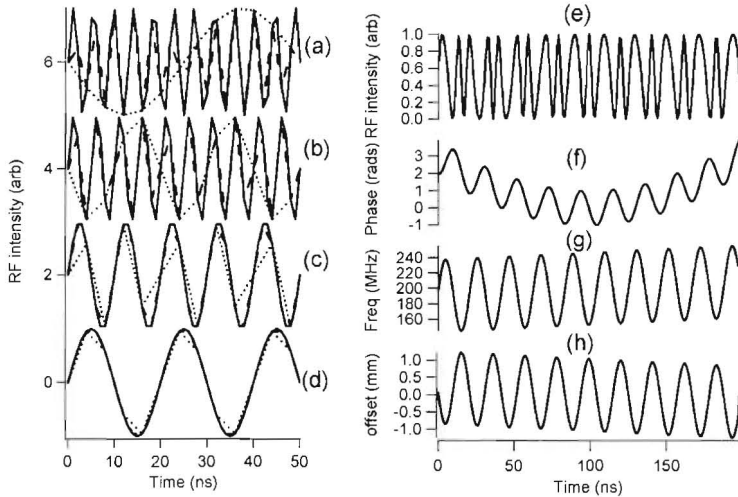
Fig. 3: Left: Calculated aliasing of an arbitrary waveform generator. From top to bottom, 250 (a), 200 (b), 100 (c), and 50 MHz (d) sine waves (offset vertically) sampled at 1 GS/s (solid) 500 MS/s (dashed) and 250 MS/s (dotted). Right: Calculated time dependent RF intensity (e), phase (f), frequency (g), and horizontal offset for a 500 mm focal length quartz pulse shaper at 267 nm (h).

Method 2 is designed to overcome the drawbacks of Method 1 at negligible additional cost and slightly increased complexity. Method 2 is diagrammed in Figure 2b, and the comparison in terms of RF frequencies is sketched in Fig. 2c. The local oscillator (LO) provides a high frequency analog waveform which can be modulated by the AWG. The AWG must be of sufficient bandwidth to cover the bandwidth of the AOM, but does not need to produce the highest frequency; for a frequency range of 150-250 MHz the peak frequency of the AWG is 150 instead of 250 MHz. Lowering the LO frequency to 250 MHz would lower the peak frequency of the AWG to 100 MHz. Since only relative phase across a single pulse matters, the LO need not be synchronized to the laser. The RF components are commercially available at low cost with simple assembly (SMA connectors). The frequencies typically used (<500 MHz) do not require special handling. Typical peak powers into the AOM transducer are in the range of 2-6 W pulsed RF, for which small, relatively low cost amplifiers are readily available.

The benefits of shaping a lower frequency waveform are illustrated in Fig. 3. Figure 3 demonstrates how amplitude is significantly modified in undersampled sinusoidal waves.

While the analog RF electronics smooth out the aliasing slightly, for cases of significant aliasing, such as 250 MHz at $\leq$500 MS/s, the RF limitations can clearly be seen on an oscilloscope.

We have employed methods 1 and 2 for comparison in this paper. Method 1 is performed by disconnecting the local oscillator and mixer and increasing the AWG center frequency. Our shaped RF waves for method 2 are 10 microsecond long 50-150 MHz RF pulses from a 1 1 GS/s AWG (Gage CompuGen11G) mixed with a 300 MHz local oscillator followed by high and low pass filters passing the 150-250 MHz sideband, before amplification to 2-6 W (all are MiniCircuits RF components: mixer ZFM-4-S, local oscillator ZX-95-400-S, high pass filter SHP-150+, low pass filter SLP-250+, amplifier ZFL-5W-1, a ZFL 500 amplifier and any required attenuators are added prior to the main amplifier to produce peak RF values between 2 and 6 W). The filters remove the fundamental frequency of the AWG, 50-150 MHz, as well as the frequency of the local oscillator, 300 MHz, and the high frequency sideband, 350-450 MHz; the various frequencies present prior to frequency filtering are illustrated in Fig. 2c.

A variable delay, low-jitter trigger is necessary to synchronize the RF pulse, and therefore the acoustic pulse, with the laser arrival at the AOM. A jitter of 10 ns will cut the effective time-bandwidth product in half, $\Delta t_{RF} = 1/(\Delta\omega_{RF}+t_{jitter})$. We use the trigger from the Spectra Physics Tsunami delay generator box (SDG II) further delayed ~997 μs with a programmable delay generator (Stanford Research DG535). This trigger exhibits a jitter of ~2 ns, measured using a sharp amplitude feature programmed into a sinusoidal RF waveform viewed on a 1 GHz scope triggered from an optical pulse from the laser.

2.4 How does a shaped RF pulse shape the optical pulse?

The relationship between the shaped RF pulse and shaped optical spectral phase and amplitude is straightforward. The acoustic wave $I_{AWG}(t)$ is represented as an intensity, $|I(t)|$, multiplied by a phase, $\varphi(t)$. The AWG provides a time dependent frequency, $v(t)$, and the translation between phase and frequency is the derivative, as in Eqn. 2.

$$I_{AWG}(t) = |I(t)|\exp(i\varphi(t))$$
$$v(t) = d\varphi(t)/dt \tag{2}$$

We will only consider the wave generated by the AWG; for method 1 the AWG waveform is the waveform in the AOM, for method 2 the AOM sees 300 MHz minus the AWG waveform, flipping the sign of the phase since we keep only the low frequency sideband.

Practically, $I_{AWG}(t)$ is a list of numbers specifying the intensity the AWG should output at each time step. From Eqn.2, a linear ramp in phase versus time has a constant slope equal to the frequency of the sine wave; 2 π radians of phase every 10 ns is a 100 MHz wave. The addition of polynomial, sinusoidal, or arbitrary phases is trivially accomplished by adding these phases to the linear ramp in $\varphi(t)$. At this point, one must ensure that the instantaneous frequency is always within the technical capabilities of the AOM.

Figure 3 gives a simple example of added phase (not showing the linear ramp, for clarity), RF waveform, and instantaneous frequency to illustrate these relations for a waveform short enough to see individual oscillations. A real AOM waveform 100 times longer than this can have 100 times more accumulated phase shift. Note in Fig. 3g that changes in phase occurring over relatively few pixels can quickly approach the frequency bandwidth limitations of the AOM, which must be considered in machine learning or adaptively controlled pulse shaping experiments.

RF amplitude shaping is performed directly using $|I(t)|$ in Eqn. 2. At this point, the RF waveform is phase and amplitude shaped in time, and therefore in space across the AOM due to the acoustic wave transit. The temporal scale from the AWG must then be transformed to a

spectral scale in the pulse shaper. One method to convert the RF timing to optical spectrum is to scan a narrow RF pulse in time and record the spectrum. A scanned RF pulse calibration is shown in Fig. 4.
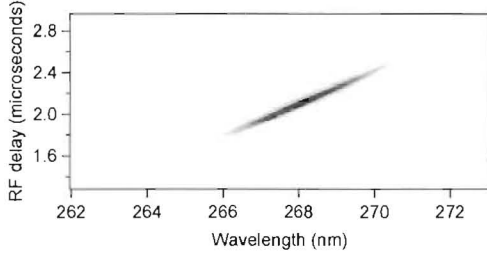

Fig. 4: Calibration of spectrometer with respect to RF wave timing. The delay of a 10 ns wide RF pulse is swept across the range of delays to find the spectral center (in RF time delay) and spectral slope with respect to RF delay, for calculation of spectral phase from time dependent RF phase.

Figure 5 presents a direct measurement of the limitations of the RF bandwidth and acoustic decay properties of two fused silica AOMs. Fig. 5a and 5b compare the fused silica Brimrose and Neos AOMs operating under RF generation Method 2. Fig. 5b and 5c compare the fused silica Neos AOM using RF generation Method 2 and Method 1, respectively. The optical signal noise measured by the standard deviation of the intensity of 4000 single laser shots was identical for the two RF generation Methods. Both Methods have the same RF bandwidth. The differences between Fig. 5b and 5c are attributed to small vertical pointing changes, with c being slightly better overlapped with the acoustic wave. The lower bandwidth of the AOM apparent in Fig. 5a, and the oscillatory structure present in Fig. 5a-c is attributed to manufacturing details of the coupling between the transducer and the crystal.
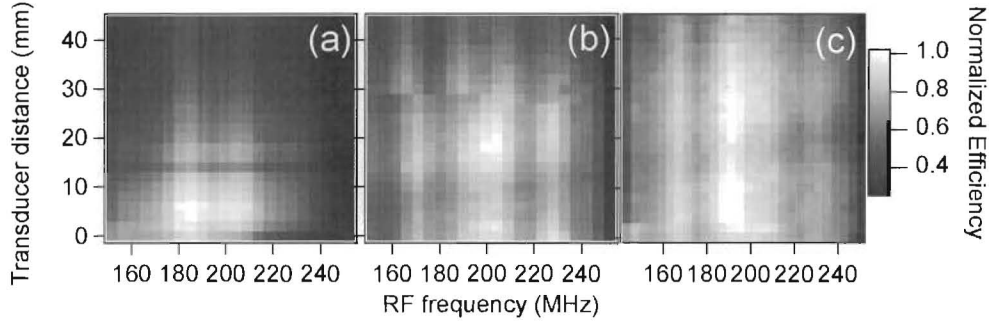
Fig. 5: Diffraction efficiency of 267 nm as a function of RF center frequency and distance from transducer for Brimrose AOM using Method 2 (a), Neos AOM using Method 2 (b), Neos AOM using Method 1 (c).

2.5 Spatial beam displacement

Laser beam pointing changes will occur at the output of an AOM as a function of spectral phase, as with any pulse shaper. For an AOM, Eqn. 3 describes the angle between the incident and diffracted beam in air, θ as a function of RF frequency, ν_{RF}, the wavelength of light, λ, and the acoustic sound speed, $u_{acoustic}$[1, 3, 22].

$$\theta = \frac{\lambda \nu_{RF}}{u_{acoustic}} \tag{3}$$

8

For a "4-f" configuration, different RF frequencies will lead to spatial beam displacements of $x_{displaced} = f \tan(\theta(\nu) - \theta(\nu_0))$. Figure 3h shows that this can be a significant spatial displacement for frequency sweeps near the limits of the AOM RF bandwidth. Figure 6 shows a direct measurement of the spatial displacement as a function of RF frequency. A spectral slice at ~267 nm with a spatial extent of ~1 mm was selected with an iris before the AOM. The diffracted beam was propagated about 1.5 m after the pulse shaper onto a line camera (ThorLabs LC1-USB) with 7 μm pixels. The line profile was recorded as a function of RF frequency, as shown in Fig. 6. The solid line is the calculation of the offset using Eqn. 3, the dashed line illustrates the prediction of Eqn. 3 for a similar shaper with an 800 nm pulse.
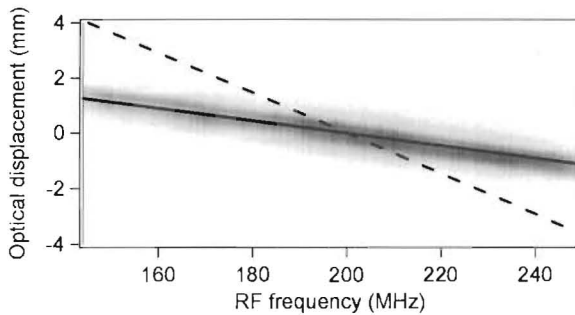
Fig. 6: Measured horizontal displacement after shaping due to change in center RF frequency for 267 nm light. Solid line is prediction from Eqn. 3, while dashed line is prediction for horizontal displacement for a TeO$_2$ AOM at 800 nm using 500 mm focal length optics.

The spectral calibration of Fig. 4 allowed large (at the maximum of the RF bandwidth) quadratic and cubic phases to be added to the linear phase ramp that generates the carrier frequency. The polynomial added phase was centered on the spectral slice being monitored; in this manner we verified that no additional diffractive effects were observable besides those contained in Eqn. 3. Equation 3 also predicts the separation of multiple diffracted wavelengths, which was verified by measuring the separation of diffracted light at 532 and 633 nm for collinear beams incident on the AOM. For AOM pulse shaping, Eqn. 3 fully describes the optical output displacement that we measured as a function of RF frequency and optical frequency.

2.6 Shaped pulse measurement

After the calibration depicted in Fig. 4 has been performed, spectral phase can be calculated from the AWG waveform. Actually, the waveform is calculated from the desired spectral phase, and simply needs calibration. Alternatively, the shaped optical pulse can be directly measured. We built a transient grating frequency resolved optical gating (TG-FROG)[23] device to measure the pulse shapes produced. Due to the narrow bandwidth of our 267 nm pulses, we used 300 μm sapphire beamsplitters (CVI UT-266-50-45-S) and neglect dispersion compensation of the reflected beams. Pulses are focused from 3 corners of a box geometry using a low scattering 1.5" diameter 4" focal length 90^0 off axis paraboloid (Newport 50338Al) into a 1 mm thick sapphire plate, overlapped in time and space. Another paraboloid collimates the output after masking off the excitation beams and scattered light before coupling into a home built spectrometer. One of the pulses is on a computer controlled delay stage, which is scanned to produce a FROG spectrogram equivalent to a third order nonlinearity self diffraction FROG. The benefits of TG-FROG are well documented[23], and allowed us to readily find the TG signal when the pulses are close to optimally compressed and >1 μJ in energy. The same aluminum mirrors, and beamsplitters can be used for measurements of pulses up to 4 ps long at 267, 400, and 800 nm. Figure 7 shows a

compressed pulse and a shaped pulse, with two different frequency sinusoidal phases added, illustrating the fidelity of the shaper described.
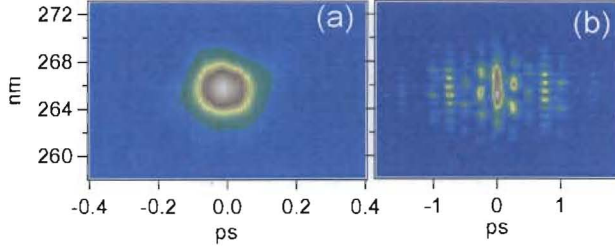

Fig. 7: Transient grating frequency resolved optical gating traces (TG-FROG) of compressed (a) and shaped (b) pulses. The shaped pulse has sine waves of two different frequencies imposed.

2.7 Considerations of broad bandwidth pulses centered at 800 nm, 400 nm, and 267 nm

One of the most important driving applications for pulse shaping is coherent control[19, 24-29]. Coherent control would clearly benefit from the largest possible laser bandwidth, to allow interference between a more extensive set of atomic or molecular eigenstates. To achieve 4000 cm^{-1} of bandwidth (e.g. full width at 5% of the maximum intensity of a 1900 cm^{-1} full width half maximum, ~8fs Gaussian transform limited pulse) at 267, 400, and 800 nm requires a total wavelength span of 28, 64, and 250 nm, respectively. This wavelength span will cause spatial offsets between the highest and lowest optical frequencies of 0.19, 0.43, and 2.35 mm. These offsets are less than the spatial shift associated with pulse shaping using 200±50 MHz of 0.89, 1.35, and 3.76 mm. These spatial shifts are proportional to the focal length of the collimation lenses, the optical bandwidth, and the frequency bandwidth of RF pulse shaping. The calculations of this paragraph use Eqn. 3 with a central RF frequency of 200 MHz, 200 mm focal length collimation lenses, and 5960 and 4260 m/s acoustic wave velocities[22] for fused silica at 267 and 400 nm, and TeO$_2$ at 800 nm, respectively. Note that it may also be possible to compensate for the static spatial shift due to broad bandwidth by insertion of a properly shaped prism, with the caveat that additional temporal dispersion would be introduced.

Diffraction efficiency is also a function of wavelength, as given by Eqn. 4, where L and H are the transducer length and height, $P_{acoustic}$ is the acoustic power in the crystal, M_2 is the Figure of Merit, and a slowly varying prefactor has been neglected[1, 3].

$$Efficiency = \sin^2(\frac{\pi}{\lambda}(\frac{LP_{acoustic}M_2}{2H})^{1/2})\sin c^2(\frac{\pi L \Delta\theta_B \nu_{RF}}{u_{acoustic}}) \qquad (4)$$

Figure 8 shows the efficiency as a function of bandwidth for L=5 mm, H=1.5 mm, $u_{acoustic}$=4260 (5960) m/s, ν_{RF}=200 MHz, M_2 =34(1.5) 10^{-15} s^3/kg[22], and $P_{acoustic}$ = 3 (5) W, with the numbers in parentheses used for the fused silica AOM at 400 and 267 nm. The Bragg angle has been set at slightly longer wavelengths to counteract the increasing efficiency of the AOM as the optical wavelength decreases. Figure 8 illustrates that diffraction efficiency bandwidths for spectrally broad pulses will be dominated by Bragg angle mismatch producing FWHM of ~220, 310, and 270 nm for 800, 400, and 267 nm central wavelengths. These broad spectral widths are currently achievable via filamentation[30, 31], hollow fiber[30, 32], or non-collinear optical parametric amplification[33] to broaden the pulses, coupled with achromatic phase matching to efficiently frequency mix into the ultraviolet. The exact AOM

10

spectral bandwidth will depend on the specific AOM optimization parameters, but this calculation provides a rough description of the effect. From Fig. 8, it is clear that 800 nm broadband pulses with bandwidth over 200 nm will be spectrally filtered, while large bandwidths at 400 and 267 nm are less problematic. Absorption is not included in the calculations. Clearly there are limitations for shaping of continuum pulses that span several hundred nanometers, but AOM shaping of sub-10 fs pulses is possible, and both spatial offsets and wavelength dependent efficiency factors become less problematic as the central optical wavelength shortens.
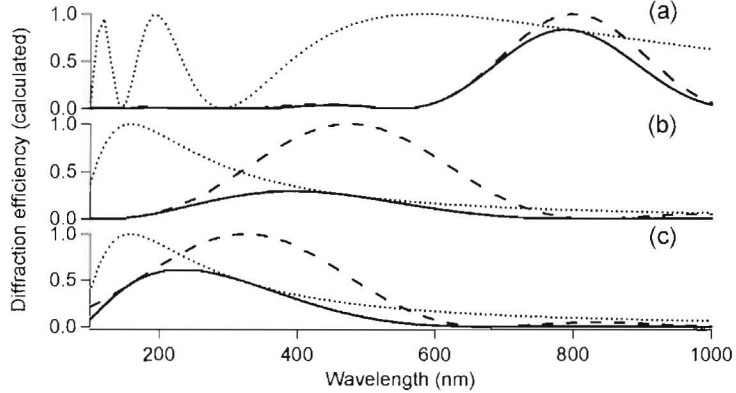
Fig. 8: Diffraction efficiencies calculated from Eqn. 4 broken down into the first term (dotted line), the second term (dashed line) and their product (solid line) for conditions appropriate for 800 (a), 400 (b), and 267 nm (c) central wavelengths.

3. Conclusion

We have considered in detail the essential elements necessary to build AOM pulse shapers from the ultraviolet to the near infrared. In particular, different methods of RF generation were compared, and technical features of commercial fused silica AOMs were reported. Considerations of the spatial shift of output pulses under the influence of differing RF central frequencies and the relationships between different RF frequencies to available pulse shaping spectral phase were detailed. Limitations of AOM pulse shaping for very broad spectral pulses were described, but it is clear that the range of optical frequencies in sub-10 fs pulses can be successfully shaped with an AOM. Also, the problems of spatial shift and wavelength dependent efficiency are reduced at shorter wavelengths, suggesting great potential for AOM pulse shaping of sub-10 fs ultrashort pulse bandwidths from 267 to 800 nm.

Acknowledgements